



Cite this: RSC Adv., 2014, 4, 30887

## Biomass-derived carbon materials for high-performance supercapacitor electrodes†

Changping Ruan,<sup>ab</sup> Kelong Ai<sup>a</sup> and Lehui Lu<sup>\*a</sup>

A low-cost and high-performance carbon material for supercapacitors is fabricated via a simple yet versatile strategy using a renewable natural resource: bean dregs. Owing to the natural properties of the heteroatom-enriched resource and the uniqueness of the fabrication approach, an optimized sample with plentiful heteroatoms (mainly O and N), well developed hierarchical porosity and highly ion-accessible surface area is obtained. The synergistic function of the heteroatom doping and the unique structural characteristics endows the as-prepared sample with an excellent combination of electric double layer capacitance and pseudo-capacitance, thus remarkably improving its electrochemical performance. As expected, it exhibits superior capacitive performance, including high specific capacitance, impressive rate performance, and excellent cycle stability. Considering the facile procedure and the easy-availability of raw material, this environmental-friendly and cost-effective method can be expected to perform extraordinarily in the widespread application of supercapacitors.

Received 13th May 2014

Accepted 10th July 2014

DOI: 10.1039/c4ra04470c

[www.rsc.org/advances](http://www.rsc.org/advances)

### 1. Introduction

Electrochemical capacitors (ECs, also known as ultracapacitors or supercapacitors), are one of the most promising energy storage devices. In recent years, they have been drawing increasing attention because of their excellent cyclability, high power density, and high charge and discharge rate.<sup>1</sup> Based on their different charge storage mechanism, there are two types of ECs: electric double layer capacitors (EDLCs) and pseudo-capacitors. EDLCs store the charge electrostatically by reversible adsorption of ions at the interface between electrolyte and active materials (nonfaradaic process). This is different from pseudo-capacitors, in which case the fast and reversible redox reaction (faradaic process) is the main charge storage mechanism. Currently, the main commercially available supercapacitors, EDLCs, use various carbon-based materials as electrode active materials, due to their extraordinary cycle stability, high power capability, low cost, easy fabrication and nontoxicity.<sup>2–10</sup> Unfortunately, carbon materials usually suffer from low energy density owing to their limited capacitance, and this limits their widespread use. Therefore, one of today's EDLC

research focuses is on further enhancing the specific capacitance of carbon materials.<sup>2–10</sup>

Incorporating heteroatoms into the carbon framework is an efficient approach for enhancing the capacitance performance of carbons. The incorporated heteroatoms have great potential for improving the capacitive nature, through providing extra pseudo-capacitance and enhancing the surface wettability and the electronic conductivity of carbons.<sup>11–25</sup> Currently, two major strategies for the preparation of the heteroatom-incorporated carbons have emerged. In the first strategy, heteroatom (mainly N) is introduced by treating carbon materials in the presence of nitrogen-rich agent (ammonia, melamine or urea) at elevated temperatures.<sup>17,18</sup> The other strategy is to carbonize heteroatom-containing precursors directly, including polypyrrole, polyacrylonitrile, melamine-formaldehyde resin, melamine diborate, *etc.*<sup>19–25</sup> Nevertheless, these two strategies are highly dependent on petrochemical sources. Their applicability is limited by the decreasing availability of fossil fuels. Therefore, it is an environment-friendly and sustainable approach to prepare the heteroatom-doped carbon material by using renewable natural resources, as it reduces the energy dependence on fossil fuels.<sup>26–31</sup> In recent years, there have been some reports on the preparation of the heteroatom-incorporated carbon materials by using renewable natural resources, such as chicken eggshell membranes,<sup>28</sup> fungi,<sup>29</sup> and D-glucosamine.<sup>30</sup> Also, our group has recently reported a novel carbon material for high-performance supercapacitors derived from bacteria.<sup>31</sup> However, only moderate improvement of capacitance in these cases has been achieved. Moreover, these resources are not widely available. Widespread application of supercapacitors may require more abundant renewable materials with easy-

<sup>a</sup>State Key Laboratory of Electroanalytical Chemistry, Changchun Institute of Applied Chemistry, Chinese Academy of Sciences, Changchun, P. R. China. E-mail: lehuilu@ciac.ac.cn; Fax: +86-43185262406; Tel: +86-43185262418

<sup>b</sup>University of Chinese Academy of Sciences, Beijing, P. R. China

† Electronic supplementary information (ESI) available: Porosity properties, elemental compositions, SEM micrographs, Raman spectra, and XRD of bean dregs derived carbons; electrochemical performance of BD-700-A3 and BP2000 in the three- and two-electrode configuration; IR drops; CVs of BD-600-A3 and BD-800-A3; galvanostatic charge/discharge curves of control A and B in the three-electrode system. See DOI: 10.1039/c4ra04470c

availability and low cost than these materials. Therefore, it is urgent to develop a high-performance electrode material for supercapacitors from more abundant renewable natural resource.

Herein, a heteroatom-enriched biomass, bean dregs, has attracted our attention. Such renewable resource is rich in carbon, nitrogen and oxygen elements owing to the existence of carbohydrates (cellulose and polysaccharides), proteins and lipids, and thus can be directly used as precursor for the production of the heteroatom-incorporated carbon materials.<sup>32–34</sup> As the main by-products of bean curd and soy milk, this material is extremely abundant. However, the utilization of such material has been barely explored, particularly in energy fields. It is reported that more than 800 000 tons of bean dregs are produced in China each year and most of them are abandoned.<sup>32</sup> To this end, we report, for the first time, the scalable preparation of a low-cost heteroatom-incorporated carbon material for supercapacitors by using bean dregs as precursor. The utilization of this abundant bio-waste is of great significance to not only explore low-cost and high-performance energy storage device, but also tackle environmental issues. In the present work, a simple yet versatile strategy is applied for the production of the high-performance carbon material. As expected, the as-prepared heteroatom-doped carbon material exhibits superior capacitive performances, including high specific capacitance, impressive rate performance, and excellent cycle stability. Therefore, it is a promising candidate for the electrode active material of high-performance supercapacitors.

## 2. Experimental section

### 2.1 Preparation of materials

A three-step strategy was used to prepare the activated carbons. Firstly, bean dregs (60 g) received from bean curd factory were mixed with deionized water (120 ml) and put into a 200 ml Teflon lined stainless autoclave, followed by hydrothermal treatment at 180 °C for 24 h. The obtained brown hydrothermal product was filtered and washed with distilled water and ethanol for several times and then dried at 120 °C in an electric oven. The following step was a pre-carbonization process: the dried brown powder was transferred into a quartz boat in a tubular furnace and then heated to 400 °C and maintained for 1 h under Ar atmosphere (at a ramp of 5 °C min<sup>-1</sup>). The last step was the activation process. The obtained black pre-carbonized products (0.4 g) were ground with a specific mass of KOH pellets in an agate mortar. The mixture was then transferred into the quartz boat in the tubular furnace and heated to the specific activation temperature and maintained for 1 h under Ar flow (at a ramp of 5 °C min<sup>-1</sup>). The non-activated sample was prepared through exactly the same procedures, except that no KOH was used. The obtained activated materials were washed thoroughly 4 times with deionized water, 3 times with HCl solution (6 mol L<sup>-1</sup>), twice with deionized water, twice with ethanol to remove any impurities. After centrifugation, the materials were dried at 120 °C in an electric oven. The as-prepared samples were denoted as BD-T-A<sub>x</sub> (BD was the abbreviation of bean dregs, T was the activation temperature, x

was referred to the mass ratio between activating agent and pre-carbonized product). The commercial carbon black BP2000 was bought from Cabot Corporation.

In the control experiment, two different two-step methods were applied to the preparation of control A and B, respectively. Control A was prepared by pre-carbonization and activation procedure without the hydrothermal treatment step. Briefly, bean dregs received from bean curd factory were washed thoroughly with ethanol and then filtered and dried at 120 °C in an electric oven. The obtained white powder was then pre-carbonized and activated through exactly the same procedures as BD-700-A3 (KOH/pre-carbonized product at a weight ratio of 3). In the case of control B, the hydrothermal product was directly activated by KOH (KOH/hydrothermal product at a weight ratio of 3) without the pre-carbonization step. Then, the obtained activated materials were washed and dried through exactly the same procedures as BD-700-A3.

### 2.2 Characterization

Scanning electron microscopy (SEM) images, Energy dispersive X-ray analysis (EDX) and elemental mappings were operated on the same instrument, using Philips XL 30 and a JEOL JSM-6700F microscope. TEM images were collected on a TECNAI G2 high-resolution transmission electron microscope. Nitrogen adsorption and desorption isotherms were measured using a QuadraChromes Adsorption Instrument at 77 K. Powder X-ray Diffraction (XRD) spectra were operated on a Bruker D8 ADVANCE diffractometer (Germany) using Cu K $\alpha$  (1.5406 Å) radiation. The X-ray photoelectron spectrum (XPS) was collected on a VG ESCALAB MKII X-ray photoelectron spectrometer using Al-K $\alpha$  as the exciting source. The contents of C, H and N element of the samples were collected on a vario EL cube elemental analysis instrument, the samples were dried at 120 °C in an electric oven through the night before testing. The Raman spectra were recorded on a HORIBA Jobin Yvon LabRAM ARA-MIS excited at 633 nm, and the sample exposure time was 10 seconds once.

### 2.3 Electrochemical measurements

The electrochemical performances were evaluated in 1 mol L<sup>-1</sup> H<sub>2</sub>SO<sub>4</sub> aqueous solution using both a three-electrode system and a symmetrical two-electrode system. The cyclic voltammogram (CV) curves and the galvanostatic charge/discharge curves were collected on a CHI 660D electrochemical work station (Shanghai CH Instruments Co., China). In the three-electrode system, the suspension of the materials (2.0 mg ml<sup>-1</sup>) was prepared by ultrasonically dispersing 5 mg carbon materials into a mixture of 2.0 ml water, 0.4 ml ethanol, and 0.1 ml Nafion (Dupont, 5 wt%). The suspension with a specific volume (5  $\mu$ l) was dropped onto the prepared glassy carbon electrode (GCE) with a diameter of 3 mm and then dried thoroughly under an infrared lamp. The GCE (unless otherwise noted) loaded with the as-prepared materials was used as the working electrode. Ag/AgCl (3 mol L<sup>-1</sup> KCl) and Pt wire were used as the reference electrode and the counter electrode, respectively.

In the two-electrode system, a composite sheet with 70 wt% as-prepared carbon samples, 20 wt% acetylene black and 10 wt% polytetrafluoroethylene (60 wt% in H<sub>2</sub>O, Sigma Aldrich, USA) was pasted on a titanium foil (by using the conductive carbon paint) to serve as the working electrode. Each composite sheet had a circular shape with the diameter of 1.2 cm. The mass of each circular sheet was between 3 and 5 mg, and the thickness of the electrode was approximately 80  $\mu$ m. Two symmetric electrodes with the same amount of active materials were immersed into 1 mol L<sup>-1</sup> H<sub>2</sub>SO<sub>4</sub> aqueous electrolyte to collect the CV curves and the galvanostatic charge/discharge curves. The 2016 coin cells were also assembled to light up the LED. Two symmetric carbon electrodes on the titanium foil were used as the working electrodes, 1 mol L<sup>-1</sup> H<sub>2</sub>SO<sub>4</sub> aqueous solution was used as the electrolyte and cellulose membrane filter with a pore diameter of 0.22  $\mu$ m as separators (the stainless steel shell was coated with gold inside). The coin cells were charged using Land battery test equipment (CT2001A).

The specific capacitances ( $C_s$ ) in the three-electrode system were calculated from galvanostatic discharge curves according to:<sup>24,28,30</sup>

$$C_s = It/mV \quad (1)$$

where  $I$  is the charge/discharge current,  $t$  is the discharge time,  $m$  is the mass of electrode active materials, and  $V$  is the voltage window.

In the two-electrode system, the specific capacitance ( $C_s$ ) of the active materials were calculated from galvanostatic discharge curves according to:<sup>5,20</sup>

$$C_s = 2It/mV \quad (2)$$

where  $I$  is the charge/discharge current,  $t$  is the discharge time,  $m$  is the mass of active materials on single electrode, and  $V$  is the voltage window. The factor of two comes from the fact that the total capacitance measured in the symmetrical two-electrode system is the sum of two equivalent single electrode capacitors in series.

### 3. Results and discussion

#### 3.1 Structure and chemical features of BD-700-A3

To optimize the experimental conditions, we prepared a series of samples by changing the amount of KOH and the activation temperature. As a result, an optimized sample BD-700-A3 with plentiful heteroatoms (mainly O and N), well developed hierarchical porosity and highly ion-accessible surface area was obtained. The morphology, microstructure and compositions of BD-700-A3 were investigated in detail. As observed in the scanning electron microscopy (SEM) images (Fig. 1a and b), the sample BD-700-A3 shows irregular shapes with the size ranging from a few to tens of micrometers. It is noteworthy that BD-700-A3 possesses not only micrometric pores on the surface, but also interconnected cavities (in the range of sub-micrometer to a few micrometers) within the texture. Contrary to BD-700-A3, the interconnected cavities are absent in the case of the non-

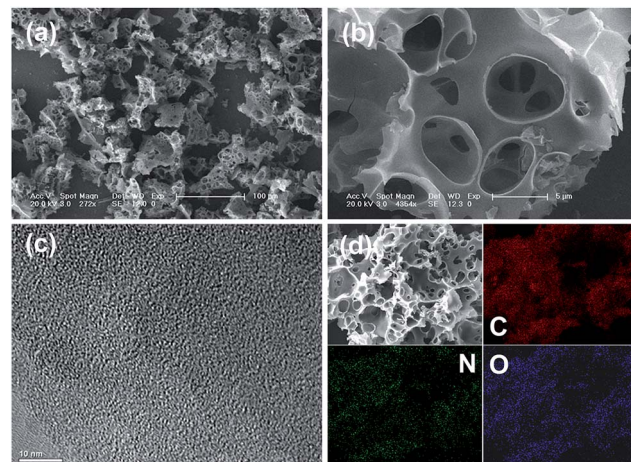


Fig. 1 SEM micrographs (a, b) and (c) high-resolution TEM image of BD-700-A3; (d) SEM image and corresponding elemental mapping images of BD-700-A3, showing the homogeneous distribution of elements: C, N and O. The scale bar in (a), (b), and (c) is 100  $\mu$ m, 5  $\mu$ m, and 10 nm, respectively.

activated sample (BD-700-A0) and the samples activated with less amount of KOH (BD-700-A1 and BD-700-A2), as evidenced by the SEM images (Fig. S1, in the ESI†). This is indicative of the occurrence of morphological transformation during the KOH activation process and demonstrates that a sufficient amount of KOH is necessary to form the interconnected cavities within the carbon texture.<sup>20,35,36</sup> It is worth mentioning that the interconnected cavities in the porous texture may serve as reservoirs for electrolyte and therefore reduce the diffusion distances of charges to the interior. Such unique textural characteristic is of great significance for fast charge transport and superior to the solid structure without space inside.<sup>37</sup> From the high-resolution transmission electron microscopy (TEM) image, we can observe that the sample has a disordered texture without graphite ribbons and crystalline impurities (Fig. 1c).<sup>20</sup> The disordered texture of the sample was further confirmed by the Raman spectra and the powder X-ray diffraction (XRD) (Fig. S2 and S3, in the ESI†). In Raman spectra, the G-band located at 1580  $\text{cm}^{-1}$  is attributed to the graphite in-plane vibrations; the D-band located at 1327  $\text{cm}^{-1}$  is associated with a double-resonance Raman process in disordered carbon. The high intensity ratio of the two peaks ( $I_d/I_g = 1.19$ ) indicates a highly disordered feature of the carbon material.<sup>20,38,39</sup> The broad width and low intensity of the 002 diffraction peak in XRD ( $\theta = 25^\circ$ ) also indicate a low degree of graphitization.<sup>38,39</sup> The N<sub>2</sub> sorption data were also collected at 77 K to investigate the porosity properties of carbon materials (Table S1 and Fig. 2). The as-prepared BD-700-A3 exhibits the type I isotherm for microporous materials and shows high N<sub>2</sub> sorption pore volume and highly developed Brunauer–Emmett–Teller specific surface area (BET-SSA, up to 2876  $\text{m}^2 \text{ g}^{-1}$ ).<sup>30,40</sup> The microporous character is further supported by the pore size distribution (PSD) based on the non-local density functional theory (NL-DFT) method. Clearly, the pores in BD-700-A3 are mainly micropores and a fraction of small mesopores in the 2–4 nm range, as reflected in Fig. 2b.

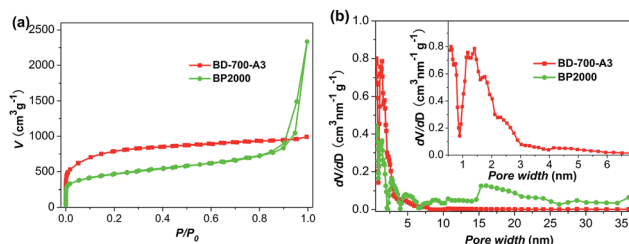


Fig. 2 (a)  $N_2$  physisorption isotherms (77 K) and (b) NL-DFT pore size distributions (PSD) of BD-700-A3 and BP2000, inset is the PSD of BD-700-A3 in the range from 0.5 to 7 nm.

The micropores are thought to be responsible for charge accommodation, while the small mesopores play a crucial role in charge transferring, especially at the high current load.<sup>2,30,36</sup>

The compositions of the as-prepared samples were analyzed by using an elemental analysis method. As presented in Table S2,† the as-prepared BD-700-A3 possesses 9.93% oxygen and 1.64% nitrogen (by weight). The detailed surface chemical compositions of the as-prepared carbon material were further revealed by X-ray photoelectron spectroscopy (XPS). The data presented in Fig. 3 agree well with the elemental analysis. The C1s peaks at 289, 286, 285.2, and 284.5 eV are attributed to C=O, C–O,  $\text{sp}^3$ -C and  $\text{sp}^2$ -C, respectively (Fig. 3a). The former two confirm the presence of oxygen functionalities in the form of carboxylic groups (COOR, 289 eV) as well as phenol and ether groups (C–OR, 286 eV).<sup>26,41</sup> The N1s peaks can be assigned to three types: N-Q (quaternary nitrogen, 401.2 eV), N-5 (pyrrolic nitrogen, 400 eV) and N-6 (pyridinic nitrogen, 398.6 eV) (Fig. 3b).<sup>42</sup> The O1s peaks at 533.7 eV and 532.4 eV provide a further evidence for the existence of oxygen functional groups in the form of C–O and C=O (Fig. 3c).<sup>43</sup> Furthermore, energy dispersive X-ray spectroscopy (EDX, Fig. 3d) and elemental mappings (Fig. 1d) were also performed to obtain more composition information and are in good accordance with the

elemental analysis and XPS results. The mapping images indicate that nitrogen and oxygen are homogeneously distributed in the carbon. Such character is probably ascribed to the highly uniform distribution and natural characteristic of the raw materials and will be beneficial for the cycle stability of the as-prepared samples.<sup>17,18,28</sup>

### 3.2 Electrochemical characters of BD-700-A3

As discussed above, the as-prepared sample BD-700-A3 possesses high BET-SSA, narrow PSD, interconnected cavities in micron scale, and abundant heteroatoms (N and O) within the carbon texture, and hence can be expected to perform excellently as electrode material for supercapacitors. In order to better characterize the electrochemical performance of the as-prepared sample and to explore the contribution of pseudo-capacitance, a three-electrode system was applied for the electrochemical measurement. The electrochemical performance of a commercial carbon black BP2000 with a BET-SSA of  $1680 \text{ m}^2 \text{ g}^{-1}$  was also investigated as a control. As shown in Fig. 4, BD-700-A3 exhibits the rectangular-like voltammetry curves and the triangular symmetric charge/discharge curves, which is typical for supercapacitors. The appearance of humps in the cyclic voltammogram (CV) curves and the transitions between 0.3 and 0.6 V in the galvanostatic curves indicate that the capacitive response generates from the combination of EDLC and pseudo-capacitance ascribed to the doped

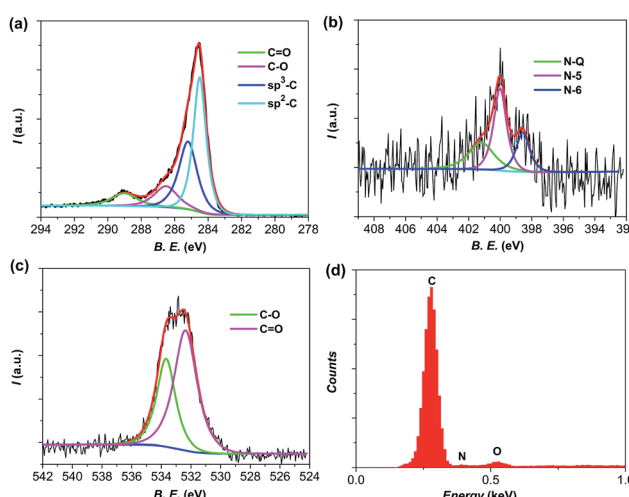


Fig. 3 Composition information of BD-700-A3: (a) C1s, (b) N1s and (c) O1s XPS spectra; (d) EDX.

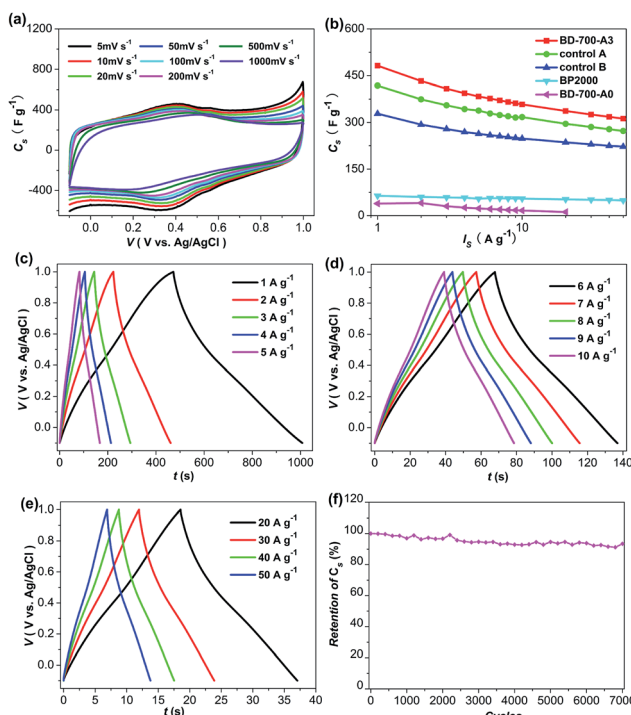


Fig. 4 Electrochemical performance of BD-700-A3 based on the three-electrode system: (a) CVs at various scan rates; (b)  $C_s$  at various current densities, compared with commercially available carbon BP2000 and some other bean dregs derived carbons; (c–e) galvanostatic charge/discharge curves collected at various current densities ( $I_s$ ); (f) capacitance retention measured at  $5 \text{ A g}^{-1}$ .

heteroatoms.<sup>11–31</sup> This is well in accordance with the high content of the oxygen and nitrogen functionalities in the as-prepared sample, as revealed by XPS. Remarkably, BD-700-A3 possesses an impressive capacitance up to  $482 \text{ F g}^{-1}$  at the current density of  $1 \text{ A g}^{-1}$ . This value is about seven times higher than that obtained from BP2000 (Fig. 4b and S4, in the ESI†). A prior literature has reported that the oxygen functional groups contributed more than 50% capacitance to the reduced graphene oxide with the O/C ratio of 10.1%.<sup>8</sup> In view of the elemental compositions of BD-700-A3 (O/C atomic ratio: 8.69%, N/C atomic ratio: 1.64%, Table S2, in the ESI†), we presume that the pseudo-capacitance associated with the heteroatom doping contributes greatly to such high specific capacitance. Moreover, as we all known, apart from extra pseudo-capacitance, the heteroatom doping may also provide further capacitive performance improvement by changing the charge distribution, improving the surface wettability and enhancing the electronic conductivity.<sup>11–31</sup> Also, the highly developed BET-SSA and the narrow PSD mainly in the micropore range of BD-700-A3 make great contribution to its high capacitance performance.<sup>30,44–49</sup> Notably, the outstanding performance of BD-700-A3 is also superior to the majority of carbon materials such as carbon nanocages ( $342 \text{ F g}^{-1}$  at  $0.1 \text{ A g}^{-1}$ ),<sup>5</sup> carbon microspheres ( $360 \text{ F g}^{-1}$  at  $5 \text{ mV s}^{-1}$ ),<sup>7</sup> hierarchical carbon materials derived from bacteria and graphene oxide ( $327 \text{ F g}^{-1}$  at  $1 \text{ A g}^{-1}$ ),<sup>31</sup> nitrogen-doped carbon nanocages derived from polyaniline ( $262 \text{ F g}^{-1}$  at  $1 \text{ A g}^{-1}$ ),<sup>39</sup> and polypyrrole-derived microporous carbon nanospheres ( $240 \text{ F g}^{-1}$  at  $100 \text{ mV s}^{-1}$ )<sup>50</sup> under the same or similar testing conditions. In contrast, the non-activated sample BD-700-A0 exhibits very poor capacitive response (Fig. 4b), in despite of its high concentration of N and O (Table S2, in the ESI†). Clearly, this is due to the poorly developed porosity and low ion-accessible surface area (Fig. S10e and Table S1, in the ESI†), suggesting that the involved reactions here are interface-bound. Therefore, a well developed porosity with high ion-accessible surface area is needed to not only form the double layer, but also generate faradaic reactions.<sup>22</sup> With regard to BP2000, the lack of heteroatom doping and the structural characteristics without optimization are likely to be the main cause of its poor capacitive response. As the larger average pore diameter (8.613 nm) and wider PSD mainly in the mesopore range for BP2000 are considered to be too wide for an efficient participation in the double layer formation (Table S1† and Fig. 2b), and thus lead to deterioration in the capacitance behaviors.<sup>2,36,44–49</sup>

Even when the scan rates increase from 5 to  $1000 \text{ mV s}^{-1}$ , the CV curves of BD-700-A3 still retain the humps-incorporated rectangular-like shapes, and the capacitive performance only suffers a little degradation (Fig. 4a). Similarly, the galvanostatic curves also exhibit excellent capacitive characteristic, as demonstrated in Fig. 4c–e. Remarkably, BD-700-A3 still has a  $C_s$  up to  $312 \text{ F g}^{-1}$  and no obvious ohmic drops ( $IR_{\text{drops}}$ ) even at the high current density of  $50 \text{ A g}^{-1}$ . Such impressive behavior is indicative of speedy dynamics of charge propagation and good rate capability.<sup>8,10</sup> This excellent rate performance is directly ascribed to the good conductivity and the well developed hierarchical porosity. That is, the good conductivity assures a good

charge propagation; the interconnected cavities serve as electrolyte reservoirs to reduce the diffusion distances of charges; while the small mesopores allow the fast ions transfer at high current load.<sup>2,26,30,37</sup> Additionally, apart from the improvement in capacitance performance, the heteroatom doping may also provoke a potential shift of the electrode.<sup>26,27</sup> As reflected in CV curves and galvanostatic curves (Fig. 4), BD-700-A3 has a stable potential window in the  $-0.1 \text{ V}$  to  $1.0 \text{ V}$  (vs. Ag/AgCl) range. This is of great significance to enhance the energy density, as it is in proportion to the square of the voltage.<sup>26</sup> The cycle life is another important property of supercapacitors. To investigate the electrochemical stability of BD-700-A3, the galvanostatic cycling was performed at the high current density of  $5 \text{ A g}^{-1}$ . At such harsh condition, the as-prepared electrode material exhibits excellent cycle stability: capacity retention can be still maintained at 93.4% after 7000 cycles (Fig. 4f). Such observation demonstrates that the pseudo-capacitance associated with the heteroatom doping is stable with cycling. The excellent cycle stability should be attributed to the unique structural feature of the as-prepared sample that N and O are firmly incorporated into the framework of the carbons.<sup>26,28</sup>

From the practical perspective, we further investigated the performance of BD-700-A3 in a symmetrical two-electrode system in  $1 \text{ mol L}^{-1} \text{ H}_2\text{SO}_4$  aqueous electrolyte. To ensure a better investigation on the feasibility of this material for commercial application, the mass loading and thickness of the electrode in the two-electrode system were comparable to the commercial level, as recommended by Ruoff's group.<sup>51</sup> As presented in Fig. 5, the quasi-rectangular CV curves and the triangular galvanostatic charge/discharge curves at various current loads are observed, which is typical for supercapacitors. Impressively, the capacitive response of BD-700-A3 in the two-electrode system ( $280.8 \text{ F g}^{-1}$  at  $0.1 \text{ A g}^{-1}$ ,  $210.2 \text{ F g}^{-1}$  at  $1 \text{ A g}^{-1}$ , Fig. 5b and c) is still impressive and comparable to

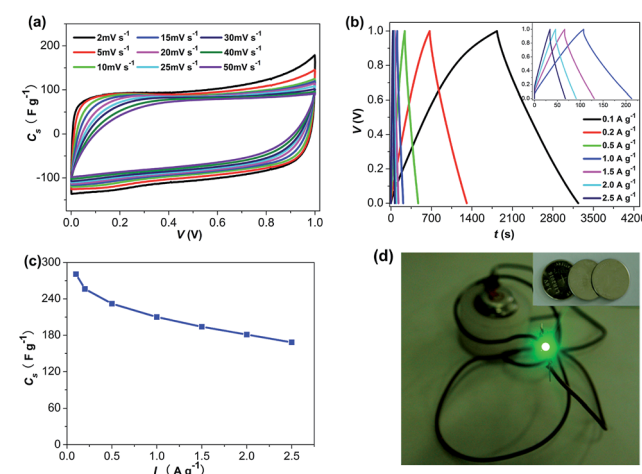


Fig. 5 Electrochemical performance of BD-700-A3 based on the two-electrode system: (a) CVs at different scan rates; (b) galvanostatic charge/discharge curves and (c)  $C_s$  at various current densities; (d) coin cell stacks made of BD-700-A3 light up a LED. The current densities were calculated based on the mass of active materials on one electrode.

many other high-performance carbon materials reported in literatures, such as carbon obtained by carbonization of sodium alginate ( $198 \text{ F g}^{-1}$  at  $2 \text{ mV s}^{-1}$ ),<sup>26</sup> carbon derived from seaweeds ( $264 \text{ F g}^{-1}$  at  $0.2 \text{ A g}^{-1}$ ),<sup>27</sup> based on the similar testing conditions. For comparison, the performance BP2000 was also investigated in the symmetrical two-electrode system under the same condition, and the results were shown in Fig. S5.<sup>†</sup> As expected, BD-700-A3 apparently indicates much larger rectangular area in CV and longer galvanostatic charge/discharge time, implying its much higher specific capacitance than that of BP2000. Furthermore, to validate the promising applications, 2016 coin cells were also fabricated by two symmetric electrodes using BD-700-A3 and titanium foils as active material and collectors. A light-emitting diode (LED) can be illuminated for dozens of seconds by a stack of coin cells (Fig. 5d).

It is interesting to note that the specific capacitances of BD-700-A3 in the two-electrode system are lower than the values obtained from the three-electrode system. It has been demonstrated that the asymmetry of the CV curves in different potential range and the non-linear galvanostatic characteristic ascribed to pseudo-capacitance will result in lower specific capacitance in the symmetrical two-electrode system than that in the three-electrode system.<sup>5,28,45,51</sup> By contrast, for EDLC, the capacitance retains unchanged in different potential range, leading to the similar capacitance performance in the two systems.<sup>52</sup> This is reasonable, as the total capacitance in the two-electrode system is determined by the component with the smaller capacitance.<sup>45</sup> In case of BD-700-A3, the pseudo-capacitance makes a great contribution to the total capacitance, thus resulting in lower specific capacitances in the symmetrical two-electrode system. Therefore, an asymmetric capacitor may be a promising alternative to achieve a better utilization of the large capacitance related to pseudo-capacitance.<sup>28,29</sup> Additionally, in our case, the different mass loading of the active material in the two systems should also be responsible for the discrepancies of capacitive values (The detailed analysis is presented in the ESI<sup>†</sup>).

### 3.3 Effect of activation condition

In order to investigate the effect of activating agent and temperature on the electrochemical behaviors, the electrochemical performances of the carbon materials activated at various conditions were compared in three-electrode system. It is worth noting that both the amount of KOH and the activation temperature play crucial roles. Changes in the activation conditions (amount of KOH and activation temperature) will lead to inferior capacitive response (Fig. 6), indicating that there is an optimum amount of KOH and a critical temperature to achieve the best capacitive nature. This is reasonable since the structure and composition of the carbon materials will be different under the various conditions (Table S1, S2, Fig. S10, in the ESI<sup>†</sup>). The detailed description about the structure and composition change is also presented in the ESI<sup>†</sup>.

We first investigated the effect of the KOH/pre-carbonized product ratio on capacitive performance, a special activation temperature of  $700 \text{ }^\circ\text{C}$  was used. As illustrated in Fig. 6a, among

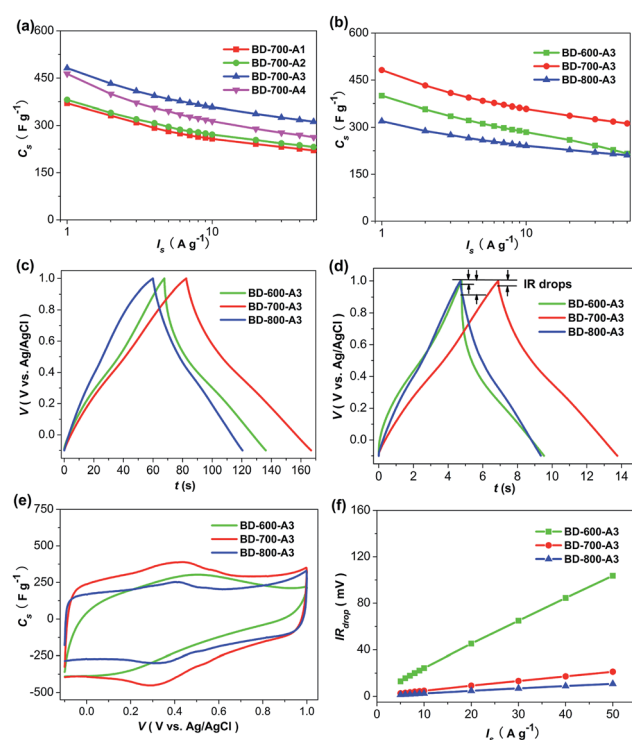


Fig. 6 Electrochemical performance comparisons of carbon materials activated at various conditions based on the three-electrode system: (a and b)  $C_s$  at various current densities; galvanostatic charge/discharge curves collected at (c)  $5 \text{ A g}^{-1}$  and (d)  $50 \text{ A g}^{-1}$ ; (e) CVs at  $200 \text{ mV s}^{-1}$ ; (f)  $IR_{\text{drops}}$  collected at various current densities.

all the tested samples, only BD-700-A3 achieves the best performance. Increasing or decreasing the amount of KOH will lead to the degradation of the electrochemical performance. It is well known that the capacitive performance is closely related to the BET-SSA, the PSD, the doped heteroatoms as well as the conductivity.<sup>2</sup> Furthermore, as mentioned before, the involved reactions here are interface-bound, and thus a well developed porosity with high ion-accessible surface area is necessary for high capacitance performance.<sup>22</sup> In view of the above mentioned facts and the structure and composition characteristics of the carbons, it is inferred that BET-SSA and PSD are likely to be the predominant origins of the different capacitive performance (Table S1 and Fig. S10, in the ESI<sup>†</sup>). More importantly, it has been illustrated that there should be an optimal pore size for microporous carbons to achieve the highest capacitance values (approximately  $0.7\text{--}0.8 \text{ nm}$  in  $\text{H}_2\text{SO}_4$  aqueous electrolyte). A narrow distribution of pore sizes close to the optimal pore size will be effective for the double layer capacitance, whereas significantly larger pores will lead to a reduced capacitance as the pores are too wide for the efficient participation in the double layer formation.<sup>30,36,44\text{--}49</sup> In our case, BD-700-A1 and BD-700-A2 possess narrower PSD than that of BD-700-A3 (Fig. S10c, in the ESI<sup>†</sup>). Apparently, such PSD is more closed to the optimal pore diameter and more desirable for a good capacitive response. Unfortunately, their much lower BET-SSA means lower ion-accessible surface area (Table S1<sup>†</sup>), thus leading to the capacitance loss (Fig. 6a). In the case of

BD-700-A4, in despite of larger BET-SSA than that of BD-700-A3 (Table S1, in the ESI†), the unexpected performance degradation indicates that the capacitance increment arising from the increased BET-SSA is smaller than the capacitance decrement from its broadened PSD. As the broadened PSD is unfavorable for an efficient utilization of the large BET-SSA and highly developed TPV (Table S1 and Fig. S10c, in the ESI†).<sup>44–49</sup> Additionally, the slightly decreased N content in BD-700-A4 may also be partly responsible for the capacitance degradation (Table S2, in the ESI†).<sup>30</sup>

Besides the amount of activating agent, activation temperature is another key factor for determining the structure and composition of the carbons and thus the capacitive nature. Therefore, we prepared another two samples BD-600-A3 and BD-800-A3, using the same amount of KOH but at different activation temperature, to study the effect of activation temperature in detail. Lowering the activation temperature, the capacitive performance of BD-600-A3 deteriorates significantly, especially at the high current load (Fig. 6b–e). As revealed in Fig. 6e and S8a (in the ESI†), the CVs of BD-600-A3 show distortion at the scan rate of 200 mV s<sup>−1</sup>, implying that the ion/electron transport is hindered.<sup>8,10</sup> Also, this is in accordance with the large IR drops (IR<sub>drops</sub>) of BD-600-A3 (Fig. 6d and f), indicating its high internal resistance and poor charge transfer capability. The lack of small mesopores that allow the fast ions transfer at high current load should be predominantly responsible for such observation.<sup>37</sup> Therefore, the insufficient development of porosity property in BD-600-A3 (including the reduced BET-SSA) should be at the origin of its poor capacitive nature. Increasing the activation temperature, the specific capacitance of BD-800-A3 is also inferior to that of BD-700-A3 (Fig. 6b–e). Apparently, the enlarged pore size, broadened PSD and the slightly reduced BET-SSA are definitely responsible for such significant performance deterioration (Table S1 and Fig. S10d, in the ESI†). In addition, higher activation temperature is likely to lead to inferior wettability, resulting in a poor pore accessibility and hence a further performance deterioration in BD-800-A3.<sup>5</sup> Additionally, the lower N content in BD-800-A3 may also be partly responsible for the capacitance degradation (Table S2, in the ESI†).<sup>30</sup> Despite the lower capacitance, the speedy dynamics of charge propagation and good rate capability of BD-800-A3 are still retained, as reflected by the rectangular-like shapes of CVs at high scan rates and the low IR drops (Fig. 6d–f and S8b, in the ESI†). Such observation is in agreement with the good mesoporosity characteristics of BD-800-A3.<sup>36,37</sup> Therefore, to optimize the capacitive performance, there should be a well balanced micro- and mesoporosity.<sup>2</sup> Based on the above analysis, it can be concluded that the impressive performance of BD-700-A3 is attributed to the synergistic function of the abundant heteroatoms and the optimal structure characteristics, suggesting the essentiality of the activation conditions.

Furthermore, as a control experiment to validate the uniqueness and the essentiality of the three-step strategy, two more samples were prepared by means of two different two-step methods, respectively. As shown in Fig. 4b and S9 (in the ESI†), the capacitive nature of the two samples is inferior to that of BD-700-A3. To understand the origin of the differences, the

composition and porosity properties of control A and B were analyzed. Considering that control A and B have similar PSD and slightly increased BET-SSA to that of BD-700-A3 (Table S1 and Fig. S11b, in the ESI†), the reduced O content is thus likely to be the key factor for the lowered capacitance (Table S2†). It is well known that the oxygen functionalities not only participate in faradaic reactions, but also improve the surface wettability.<sup>26,27</sup> Moreover, control B has a distinct morphology from that of BD-700-A3 (Fig. S12, in the ESI†), possessing a cracked and irregular shape without interconnected cavities present in the overall texture (control A exhibits a similar morphology to that of BD-700-A3, data not shown). It is rational to presume that the lack of interconnected cavities is also responsible for the lowest capacitance of control B among these three samples, as the interconnected cavities may serve as reservoirs for electrolyte and therefore reduce the diffusion distances of charges to the interior.<sup>37</sup> Taking into account that these three samples were synthesized *via* different approach, we conclude that the three-step strategy is crucial for retaining a sufficiently high content of oxygen in the carbon framework. To the best of our knowledge, there have been no reports about the utilization of such three-step strategy. During the hydrothermal treatment, the bean dregs may go through a series of reactions: hydrolysis, dehydration, polymerization, and aromatization, thus a hydrothermal product with a high concentration of oxygen groups incorporated into the framework was obtained.<sup>30,35</sup> In the pre-carbonization procedure, some unstable component is likely to decompose and the hydrothermal product may go through a further polymerization step to form a firm and stable framework with a moderate amount of O and N retained. It is apparent that only BD-700-A3 can maintain a high concentration of O, as well as the well developed hierarchical porosity. Such features are remarkably beneficial to electrochemical performance.

## 4. Conclusion

In summary, we have proposed and demonstrated that the bio-waste bean dregs can be converted into superior carbon material for high-performance supercapacitors by a unique three-step strategy. The impressive capacitive response of the optimal sample is strongly related to its unique features of composition and structure, including the high BET-SSA, the well developed hierarchical porosity and the presence of abundant heteroatoms. Considering the facile approach and the abundant bean dregs abandoned in daily life and manufacture process, this environmental-friendly and cost-effective strategy can be expected to perform extraordinarily in the widespread application of supercapacitors. Furthermore, this facile approach may hold great promise in some other energy fields, such as hydrogen storage, oxygen reduction reaction and lithium ion battery.

## Acknowledgements

Financial support by NSFC (no. 21125521) and the National Basic Research Program of China (973 Program, no. 2010CB933600) is gratefully acknowledged.

## Notes and references

1 B. E. Conway, *Electrochemical Supercapacitors: Scientific Fundamentals and Technological Applications*, Plenum Press, New York1999.

2 P. Simon and Y. Gogotsi, *Nat. Mater.*, 2008, **7**, 845–854.

3 J. R. Miller and P. Simon, *Science*, 2008, **321**, 651–652.

4 Y. P. Zhai, Y. Q. Dou, D. Y. Zhao, P. F. Fulvio, R. T. Mayes and S. Dai, *Adv. Mater.*, 2011, **23**, 4828–4850.

5 K. Xie, X. T. Qin, X. Z. Wang, Y. N. Wang, H. S. Tao, Q. Wu, L. J. Yang and Z. Hu, *Adv. Mater.*, 2012, **24**, 347–352.

6 A. Izadi-Najafabadi, S. Yasuda, K. Kobashi, T. Yamada, D. N. Futaba, H. Hatori, M. Yumura, S. Iijima and K. Hata, *Adv. Mater.*, 2010, **22**, E235–E241.

7 H. Kim, M. E. Fortunato, H. X. Xu, J. H. Bang and K. S. Suslick, *J. Phys. Chem. C*, 2011, **115**, 20481–20486.

8 Z. B. Lei, N. Christov and X. S. Zhao, *Energy Environ. Sci.*, 2011, **4**, 1866–1873.

9 Y. W. Zhu, S. Murali, M. D. Stoller, K. J. Ganesh, W. W. Cai, P. J. Ferreira, A. Pirkle, R. M. Wallace, K. A. Cychosz, M. Thommes, D. Su, E. A. Stach and R. S. Ruoff, *Science*, 2011, **332**, 1537–1541.

10 Z. B. Lei, L. Lu and X. S. Zhao, *Energy Environ. Sci.*, 2012, **5**, 6391–6399.

11 H. Nishihara and T. Kyotani, *Adv. Mater.*, 2012, **24**, 4473–4498.

12 Z. S. Wu, A. Winter, L. Chen, Y. Sun, A. Turchanin, X. L. Feng and K. Müllen, *Adv. Mater.*, 2012, **24**, 5130–5135.

13 C. O. Ania, V. Khomenko, E. Raymundo-Piñero, J. B. Parra and F. Béguin, *Adv. Funct. Mater.*, 2007, **17**, 1828–1836.

14 W. Li, F. Zhang, Y. Q. Dou, Z. X. Wu, H. J. Liu, X. F. Qian, D. Gu, Y. Y. Xia, B. Tu and D. Y. Zhao, *Adv. Energy Mater.*, 2011, **1**, 382–386.

15 Z. H. Wen, X. H. Wang, S. Mao, Z. Bo, H. Kim, S. M. Cui, G. H. Lu, X. L. Feng and J. H. Chen, *Adv. Mater.*, 2012, **24**, 5610–5616.

16 Y. Zhao, C. G. Hu, Y. Hu, H. H. Chen, G. Q. Shi and L. T. Qu, *Angew. Chem., Int. Ed.*, 2012, **51**, 11371–11375.

17 D. Hulicova-Jurcakova, M. Kodama, S. Shiraishi, H. Hatori, Z. H. Zhu and G. Q. Lu, *Adv. Funct. Mater.*, 2009, **19**, 1800–1809.

18 D. Hulicova-Jurcakova, M. Seredych, G. Q. Lu and T. J. Bandosz, *Adv. Funct. Mater.*, 2009, **19**, 438–447.

19 F. Beguin, K. Szostak, G. Lota and E. Frackowiak, *Adv. Mater.*, 2005, **17**, 2380–2384.

20 L. Wei, M. Sevilla, A. B. Fuertes, R. Mokaya and G. Yushin, *Adv. Funct. Mater.*, 2012, **22**, 827–834.

21 E. Iyyamperumal, S. Y. Wang and L. M. Dai, *ACS Nano*, 2012, **6**, 5259–5265.

22 H. Zhu, X. L. Wang, X. X. Liu and X. R. Yang, *Adv. Mater.*, 2012, **24**, 6524–6529.

23 F. W. Ma, H. Zhao, L. P. Sun, Q. Li, L. H. Huo, T. Xia, S. Gao, G. S. Pang, Z. Shi and S. H. Feng, *J. Mater. Chem.*, 2012, **22**, 13464–13468.

24 L. F. Chen, X. D. Zhang, H. W. Liang, M. G. Kong, Q. F. Guan, P. Chen, Z. Y. Wu and S. H. Yu, *ACS Nano*, 2012, **6**, 7092–7102.

25 K. L. Ai, Y. L. Liu, C. P. Ruan, L. H. Lu and G. Q. Lu, *Adv. Mater.*, 2013, **25**, 998–1003.

26 E. Raymundo-Piñero, F. Leroux and F. Béguin, *Adv. Mater.*, 2006, **18**, 1877–1882.

27 E. Raymundo-Piñero, M. Cadek and F. Béguin, *Adv. Funct. Mater.*, 2009, **19**, 1032–1039.

28 Z. Li, L. Zhang, B. S. Amirkhiz, X. H. Tan, Z. W. Xu, H. L. Wang, B. C. Olsen, C. M. B. Holt and D. Mitlin, *Adv. Energy Mater.*, 2012, **2**, 431–437.

29 H. Zhu, X. L. Wang, F. Yang and X. R. Yang, *Adv. Mater.*, 2011, **23**, 2745–2748.

30 L. Zhao, L. Z. Fan, M. Q. Zhou, H. Guan, S. Y. Qiao, M. Antonietti and M.-M. Titirici, *Adv. Mater.*, 2010, **22**, 5202–5206.

31 H. M. Sun, L. Y. Cao and L. H. Lu, *Energy Environ. Sci.*, 2012, **5**, 6206–6213.

32 Fermentation technology of bean dregs, <http://baike.baidu.com/view/3107492.htm>, accessed September 2011.

33 C. Z. Zhu, J. F. Zhai and S. J. Dong, *Chem. Commun.*, 2012, **48**, 9367–9369.

34 W. Xing, C. Liu, Z. Y. Zhou, L. Zhang, J. Zhou, S. P. Zhuo, Z. F. Yan, H. Gao, G. Q. Wang and S. Z. Qiao, *Energy Environ. Sci.*, 2012, **5**, 7323–7327.

35 M. Sevilla, A. B. Fuertes and R. Mokaya, *Energy Environ. Sci.*, 2011, **4**, 1400–1410.

36 L. Wei, M. Sevilla, A. B. Fuertes, R. Mokaya and G. Yushin, *Adv. Energy Mater.*, 2011, **1**, 356–361.

37 D. W. Wang, F. Li, M. Liu, G. Q. Lu and H. M. Cheng, *Angew. Chem., Int. Ed.*, 2008, **47**, 373–376.

38 H. M. Sun, W. H. He, C. H. Zong and L. H. Lu, *ACS Appl. Mater. Interfaces*, 2013, **5**, 2261–2268.

39 Y. M. Tan, C. F. Xu, G. X. Chen, Z. H. Liu, M. Ma, Q. J. Xie, N. F. Zheng and S. Z. Yao, *ACS Appl. Mater. Interfaces*, 2013, **5**, 2241–2248.

40 S. Brunauer, P. Emmett and E. Teller, *J. Am. Chem. Soc.*, 1938, **60**, 309–319.

41 K. L. Ai, Y. L. Liu, L. H. Lu, X. L. Cheng and L. H. Huo, *J. Mater. Chem.*, 2011, **21**, 3365–3370.

42 Y. J. Kim, Y. Abe, T. Yanagiura, K. C. Park, M. Shimizu, T. Iwazaki, S. Nakagawa, M. Endo and M. S. Dresselhaus, *Carbon*, 2007, **45**, 2116–2125.

43 Y. Q. Wang, F. Q. Zhang and P. M. A. Sherwood, *Chem. Mater.*, 2001, **13**, 832–841.

44 J. Chmiola, G. Yushin, Y. Gogotsi, C. Portet, P. Simon and P. L. Taberna, *Science*, 2006, **313**, 1760–1763.

45 E. Raymundo-Piñero, K. Kierzek, J. Machnikowski and F. Béguin, *Carbon*, 2006, **44**, 2498–2507.

46 D. Hulicova-Jurcakova, A. M. Puziy, O. I. Poddubnaya, F. Suárez-García, J. M. D. Tascón and G. Q. Lu, *J. Am. Chem. Soc.*, 2009, **131**, 5026–5027.

47 C. R. Pérez, S. H. Yeon, J. Ségalini, V. Presser, P.-L. Taberna, P. Simon and Y. Gogotsi, *Adv. Funct. Mater.*, 2013, **23**, 1081–1089.

48 C. Largeot, C. Portet, J. Chmiola, P. L. Taberna, Y. Gogotsi and P. Simon, *J. Am. Chem. Soc.*, 2008, **130**, 2730–2731.

49 J. Chmiola, C. Largeot, P.-L. Taberna, P. Simon and Y. Gogotsi, *Angew. Chem., Int. Ed.*, 2008, **47**, 3392–3395.

50 F. B. Su, C. K. Poh, J. S. Chen, G. W. Xu, D. Wang, Q. Li, J. Y. Lin and X. W. Lou, *Energy Environ. Sci.*, 2011, **4**, 717–724.

51 M. D. Stoller and R. S. Ruoff, *Energy Environ. Sci.*, 2010, **3**, 1294–1301.

52 L. L. Zhang, X. Zhao, M. D. Stoller, Y. W. Zhu, H. X. Ji, S. Murali, Y. P. Wu, S. Perales, B. Clevenger and R. S. Ruoff, *Nano Lett.*, 2012, **12**, 1806–1812.